Geophysical Research Letters

RESEARCH LETTER
10.1029/2021GL096574

Origins of the Intraseasonal Variability of East Asian Summer Precipitation

Qiaoling Ren[1], Fei Liu[1], Bin Wang[2], Song Yang[1], Hui Wang[1], and Wenjie Dong[1]

[1]School of Atmospheric Sciences Sun Yat-sen University, Guangdong Province Key Laboratory for Climate Change and Natural Disaster Studies, and Southern Marine Science and Engineering Guangdong Laboratory, Zhuhai, China, [2]Department of Atmospheric Sciences and International Pacific Research Center, University of Hawaii at Manoa, Honolulu, HI, USA

Key Points:

- Community Earth System Model performs well in simulating the leading intraseasonal variability (ISV) modes of East Asian summer precipitation (EASP) and their preceding tropical and mid-to-high latitude signals
- Tropical and mid-to-high latitude forcings together contribute half of the total variance of the two leading ISV modes of EASP
- External tropical and mid-to-high latitude forcings affect EASP ISV more apparently on a regional, rather than a local, spatial scale

Supporting Information:

Supporting Information may be found in the online version of this article.

Correspondence to:

F. Liu,
liufei26@mail.sysu.edu.cn

Citation:

Ren, Q., Liu, F., Wang, B., Yang, S., Wang, H., & Dong, W. (2022). Origins of the intraseasonal variability of East Asian summer precipitation. *Geophysical Research Letters*, *49*, e2021GL096574. https://doi.org/10.1029/2021GL096574

Received 18 OCT 2021
Accepted 23 JAN 2022

Author Contributions:

Conceptualization: Qiaoling Ren, Fei Liu
Data curation: Qiaoling Ren
Formal analysis: Qiaoling Ren, Fei Liu, Hui Wang
Funding acquisition: Fei Liu, Bin Wang, Song Yang, Wenjie Dong
Investigation: Qiaoling Ren, Fei Liu, Bin Wang, Song Yang, Hui Wang, Wenjie Dong
Methodology: Qiaoling Ren, Fei Liu, Hui Wang

Abstract Accurate subseasonal prediction of East Asian summer precipitation (EASP) requires a deep understanding of the origins of its intraseasonal variability (ISV). However, the relative contributions to the EASP ISV from local processes, tropical intraseasonal oscillation (ISO), and extratropical influence remain unknown. We conducted a set of numerical experiments with a grid nudging method to confirm the roles of external forcing from mid-to-high latitude wave trains and tropical ISO and quantify their relative contributions. The Community Earth System Model can reproduce realistic EASP ISV and associated preceding signals. The tropical and mid-to-high latitude forcings account for, respectively, 53% and 40% of the total variance for the two leading ISV modes of EASP. The tropical forcing contributes more significantly to the two leading modes (31% and 40%, respectively) compared to the extratropical forcing (24% and 15%). These external forcings mainly affect EASP regional averages rather than the values of local (grid) scale.

Plain Language Summary East Asian summer monsoon precipitation exhibits significant fluctuations on a 2–5-week time scale beyond the synoptic scale. These fluctuations are called intraseasonal variability (ISV). Since East Asia is located in between the largest continent (Eurasia) and the largest ocean (the Pacific), its ISV is affected by the southeastward propagating high-latitude disturbances (wave trains) and northwestward propagating tropical ISV. However, the relative roles of these outside influences have never been quantified. We applied a climate model that could reproduce realistic ISV and designed a suite of numerical experiments to quantitatively determine the contributions of these "external forcings" to the East Asian ISV. About one half of the total intraseasonal variance (a measure of ISV intensity) arises from the mid-to-high latitude and tropical forcings. Thus, accurate simulations of tropical ISV and mid-to-high latitude wave trains are critical for improving subseasonal prediction over East Asia.

1. Introduction

East Asian summer precipitation (EASP) displays salient intraseasonal variability (ISV). For example, the record-breaking Meiyu in 2020 was related to the phase change of ISV (Ding et al., 2021; B. Liu et al., 2020a). The most significant flood over East China in 1991 was also argued to be caused by strong ISV (Mao & Wu, 2006). Although ISV is the dominant source of subseasonal predictability (Meehl et al., 2021; Vitart et al., 2017), our understanding of EASP ISV, especially its origins from external forcings in the tropical and mid-to-high latitudes or from local oscillation, remains limited.

In the tropics, ISV mainly originates from the Madden-Julian Oscillation (MJO; Madden & Julian, 1971) and its boreal-summer component (B. Wang et al., 2009; Lee et al., 2013), and from the higher-frequency quasi-biweekly oscillation (Jia & Yang, 2013; Jia et al., 2013; Kikuchi & Wang, 2009). In the mid-to-high latitudes, ISV also originates from the wave train (Blackmon et al., 1984; Simmons et al., 1983; Zhang et al., 2012).

Previous studies mainly related the origins of EASP ISV to tropical forcing (Chen et al., 2001; Liang & Ding, 2012; Mao & Chan, 2005; Yang et al., 2010) or mid-to-high latitude forcing (Gao et al., 2018; Yang et al., 2017), or both (F. Liu et al., 2020; Yang et al., 2010). However, all these studies were based on lead-lag correlation analysis, which can only show the relationship between the mid-to-high latitude and tropical signals and the EASP ISV but cannot determine whether there is a causality since they may be contemporaneous. If there is a causality, this method also cannot tell which one is the cause since EASP can also significantly change the mid-to-high latitude circulation (F. Liu & Wang, 2013). It is also impossible to quantify the relative roles of these external forcings on EASP ISV using observational analysis.

Project Administration: Fei Liu
Resources: Qiaoling Ren
Software: Qiaoling Ren, Hui Wang
Supervision: Fei Liu, Bin Wang, Song Yang, Wenjie Dong
Validation: Qiaoling Ren, Fei Liu
Visualization: Qiaoling Ren, Fei Liu
Writing – original draft: Qiaoling Ren, Fei Liu
Writing – review & editing: Qiaoling Ren, Fei Liu, Bin Wang, Song Yang, Hui Wang, Wenjie Dong

EASP exhibits multiscale spatial variability. So, at what scale do these external forcings affect EASP ISV? Previous studies mainly focused on different regions, such as the Yangtze River (Gao et al., 2018; Huang et al., 2008; Yang et al., 2010), South China (P. Ren et al., 2018), Southeast China (Cao et al., 2012; Wei et al., 2017), and the Tibetan Plateau (M. Wang et al., 2018; Yang et al., 2017). It is unclear how much the external forcings affect EASP ISV on regional or more localized scales.

A case study by using a regional model was tried to understand the roles of these external forcings (Qi et al., 2019). In this study, we performed sensitivity experiments using the Community Earth System Model (CESM) to block external forcings from the mid-to-high latitudes and the tropics via a grid nudging method. The knowledge gained from this study should advance our understanding of the origins of EASP ISV.

2. Data and Methods

2.1. Model Experiments

This study used the CESM version 1.2.2 model (Hurrell et al., 2013), and ran a component set "F_AMIP_CAM5" in the CESM with a 0.9° × 1.25° (latitude by longitude) resolution and a hybrid vertical coordinate of 30 levels, in which the Community Atmosphere Model version 5 is coupled with the Community Land Model version 4.0. Monthly Hadley-OI sea-surface temperature (SST) and sea-ice concentration data (Hurrell et al., 2008) were used to drive the model, following the Atmospheric Model Intercomparison Project (AMIP) protocol (Gates, 1992). The ISV signals associated with daily-to-intraseasonal SST changes were not considered here. A full air-sea coupled CESM or AMIP runs forced by daily SST should be used to correctly simulate the tropical intraseasonal oscillation (ISO) forcing in the future, due to the important air-sea interaction in ISO simulation (DeMott et al., 2015).

To block mid-to-high latitude and tropical forcings, we performed a set of sensitivity experiments using the grid nudging method (Q. Ren et al., 2021). The synoptic-to-intraseasonal variability in the nudging area was suppressed through constraining the simulated daily horizontal wind and air temperature toward their corresponding climatological annual cycles in the whole atmosphere. This climatological annual cycle is defined as the annual average plus the first four Fourier harmonics of daily climatology, whose periods are 365 days, 182.5 days, 121.7 days, and 91.3 days, respectively (Lorenz & Hartmann, 2001). To identify the relative contributions of tropical, mid-to-high latitude, and monsoon-latitude atmospheric ISVs to EASP ISV, we performed one control experiment (CTL) and three sensitivity experiments. CTL was freely integrated according to the default setting, and its climatological annual cycle was used to nudge the following: (a) tropical belt from 15°S to 15°N in no tropical forcing (NT) experiment, (b) midlatitude belt from 45° to 50°N in no mid-to-high latitude forcing (NM) expersiment, and (c) both mid-latitude and tropical belts in no mid-to-high latitude and tropical forcings (NMT) experiment (see Table 1). All experiments were run for the period from 1979 to 2005, and the grid nudging method was applied throughout the whole year. The differences between CTL and sensitivity experiments represent the contributions of tropical and/or mid-to-high latitude forcings to the EASP ISV.

To manifest the effect of grid nudging method on horizontal wind, we first checked the climatic atmospheric eddy kinetic energy, $EKE = \int((u-\bar{u})^2 + (v-\bar{v})^2)dp$, calculated from the daily anomalies based on the climatological annual cycle of horizontal winds ($\bar{u}$, $\bar{v}$) (Figure S1 in Supporting Information S1). The EKE differences between sensitivity experiments and CTL suggest that the grid nudging method can effectively suppress the atmospheric winds in the nudging area (Figure S1 in Supporting Information S1). The relevant changes in summer-mean EASP highlight the importance of atmospheric ISV for summer precipitation (Figure S2 in Supporting Information S1). The climatic precipitation change should be sensitive to the nudging area (Q. Ren et al., 2021). The positive EASP anomaly moved northward when we moved the midlatitude nudging area northward slightly; our results on the ISV, however, were not changed qualitatively (not shown). The changes in climatic EASP are not discussed since we mainly focus on ISV here.

2.2. Observation and Reanalysis Data

To verify the model's simulation of EASP ISV, we used the high-resolution (0.25°) gridded daily precipitation over "Monsoon-Asia" from the Asian Precipitation Highly Resolved Observational Data Integration Toward Evaluation (APHRODITE) data set (APHRO_MA_025deg_V1003R1) from 1979 to 2005 (Yatagai et al., 2012),

Table 1
Control Experiment (CTL) Run and Three Sensitivity Runs With the Community Earth System Model

Exp	Nudging area	EOF1	EOF2
CTL	None	0.59	0.62
NT	15°S–15°N	0.41 (−30.5%*)	0.37 (−40.3%**)
NM	45°–50°N	0.45 (−23.7%*)	0.53 (−14.5%)
NMT	15°S–15°N, 45°–50°N	0.28 (−52.5%**)	0.37 (−40.3%**)

Note. The sensitivity runs are without tropical forcing (NT), without mid-to-high latitude forcing (NM), and without both mid-to-high latitude and tropical forcings (NMT). The nudging areas for sensitivity experiments are listed. Relative intraseasonal variability (ISV) intensity, represented by the variance of each time series projected onto CTL in the 8–40-day intraseasonal band, is shown for the two leading ISV modes of East Asian summer precipitation. Their percentage changes with respect to CTL are listed in parentheses.

* and ** indicate anomalies significant at the 95% and 99% confidence level, respectively.

which incorporates rain gauge data. Due to the lack of long-term observational precipitation in the tropical oceans, daily outgoing longwave radiation (OLR) data with a resolution of 1° × 1° from the National Oceanic and Atmospheric Administration Climate Data Record was used to represent the organized deep convection in the tropics (Lee et al., 2013; Wheeler & Hendon, 2004). For observational atmospheric circulation, we used daily winds with a resolution of 1.5° × 1.5° from the European Centre for Medium-range Weather Forecasts interim reanalysis (ERA-Interim; Dee et al., 2011).

2.3. Statistical Method

Following previous studies (F. Liu et al., 2020b; Yang et al., 2010), we obtained the ISV anomaly by removing the daily climatology, then removed synoptic fluctuations through 5-day running mean. We also applied the 8–80-day Butterworth bandpass filter to isolate the ISV anomaly, and obtained similar results (not shown).

To identify the dominant modes of EASP ISV, empirical orthogonal function (EOF) analysis was performed on the daily summer (June–August) intraseasonal precipitation anomaly over East Asia (20°–45°N, 105°–145°E) from 1979 to 2005 using both observations and CTL output. The obtained principal component (PC) was normalized by its standard deviation, and EOF pattern was scaled by multiplying this standard deviation. To outline the changes of the amplitude and preceding signals of the dominant ISV modes in the sensitivity experiments, we projected their intraseasonal precipitation anomalies onto the leading EOF modes in CTL to obtain the projected time series.

Spectral analysis was performed on each PC or projected time series to calculate the power spectrum of each dominant ISV mode. We calculated the power spectrum for each of these 27 summers from 1979 to 2005, and then studied the multiyear average. Statistical significance of the power spectrum was based on the power spectrum of red noise (Gilman et al., 1963). The intensity of these leading ISV modes was defined by the variance of the PCs or the projected time series. When the power spectra are shown in an area-conserving format, that is, the logarithm of frequency versus the product of power and frequency, the variance for each considered frequency band is proportional to the area on this type of spectral map (Wheeler & Hendon, 2004; Zangvil, 1977). Significant tests for the differences of ISV variance between sensitivity experiments and CTL were based on the Student's two-sided *t*-test (Livezey & Chen, 1983).

To detect the potential predictability sources for these ISV modes, lagged regression maps were calculated against the PCs or the projected time series, and the effective degree of freedom was calculated for the Student's two-sided *t*-test.

3. Results

3.1. Observed and Simulated EASP ISV

In observation, the two leading EOF modes of EASP ISV, explaining 10.3% and 9.8% of the total ISV variance, respectively, are significantly distinguishable from the other lower modes based on the rule of North et al. (1982). The first EOF mode exhibits a dipolar band structure with positive precipitation anomalies over the whole Southeast China to the region south of the Yangtze River and South Japan, and weak negative anomalies to the region north of the Yangtze River (Figure 1a). The second mode, however, exhibits a contrast between the wet middle and lower reaches of the Yangtze River and South Japan and the dry coastal region of Southeast China (Figure 1b), consistent with previous observations (F. Liu et al., 2020b). These two observed leading modes of EASP ISV are dominated by a significant period from 8 to 35 days, peaking at 30, 15, and 10 days for EOF1 and at 23, 15, and, 10 days for EOF2 (Figure 1c).

The CTL of CESM can simulate these two observed leading ISV modes very well, explaining 14.3% and 13% of the total intraseasonal variance of EASP, respectively. The leading ISV mode in CTL also exhibits a dipolar band structure, although the negative precipitation anomalies are a little stronger than the observation (Figure 1d). The

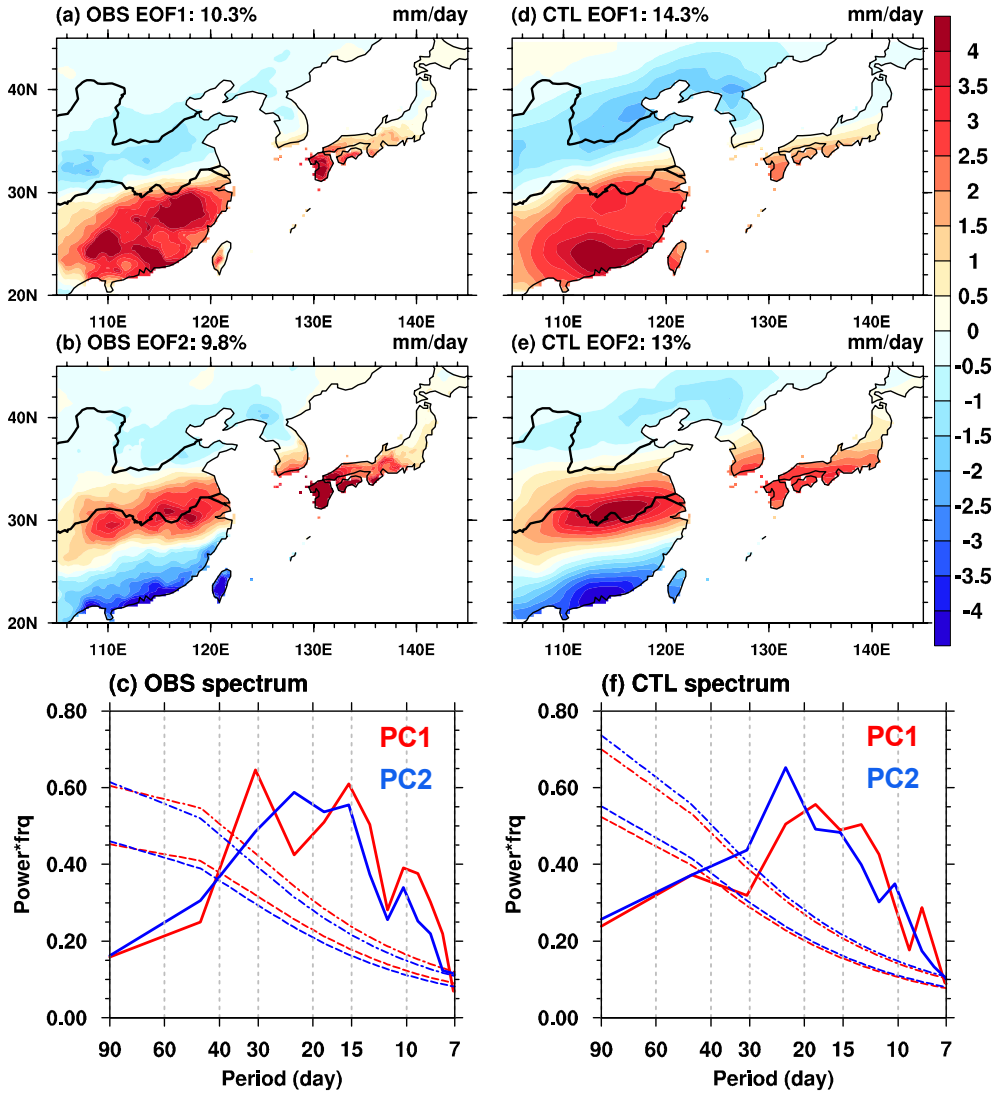

Figure 1. Observed and simulated leading intraseasonal variability (ISV) modes of East Asian summer precipitation. (a) First empirical orthogonal function (EOF) pattern of intraseasonal precipitation anomaly (mm day^{-1}) over East Asia (20°–45°N, 105°–145°E) land areas in the boreal summers (June to August) from 1979 to 2005. The upper and lower thick curves denote the Yellow River and the Yangtze River, respectively. The percentage variance accounted for by each mode is marked in the upper left corner. The intraseasonal anomaly is obtained by removing the daily climatology and then by performing 5-day running mean. (b) Second EOF. (c) Power spectra of the first (red) and second (blue) principal components of the two leading ISV modes averaged for the 27 summers from 1979 to 2005. Dashed and dot-dashed lines denote the Markov red noise spectrum and the 95% confidence level, respectively. (d)–(f) Same as (a)–(c), except for CTL.

simulated second wet-dry contrast mode coincides with the observation, with positive precipitation anomalies over the middle and lower reaches of the Yangtze River and South Japan and negative anomalies over Southeast China (Figure 1e). The periods of the two simulated ISV modes are significant from 8 to 30 days, with their peaks at 18, 13, and 8 days for EOF1 and at 23, 15, and 10 days for EOF2 (Figure 1f). Since the spectra of observed and simulated leading ISV modes are mainly significant from 8 to 40 days, we focus on this 8–40-day ISV in the following investigations.

In both observations and simulations, the first two leading modes have similar contributions to the total variance, demonstrating that they usually depict a propagating mode, as they act on the eastward propagating MJO (Wheeler & Hendon, 2004) and northeastward propagating boreal-summer ISO (Lee et al., 2013). These two leading modes of EASP also exhibit southeastward propagation, especially in early summer (F. Liu et al., 2020), but we will not discuss this seasonal evolution of EASP ISV in this paper.

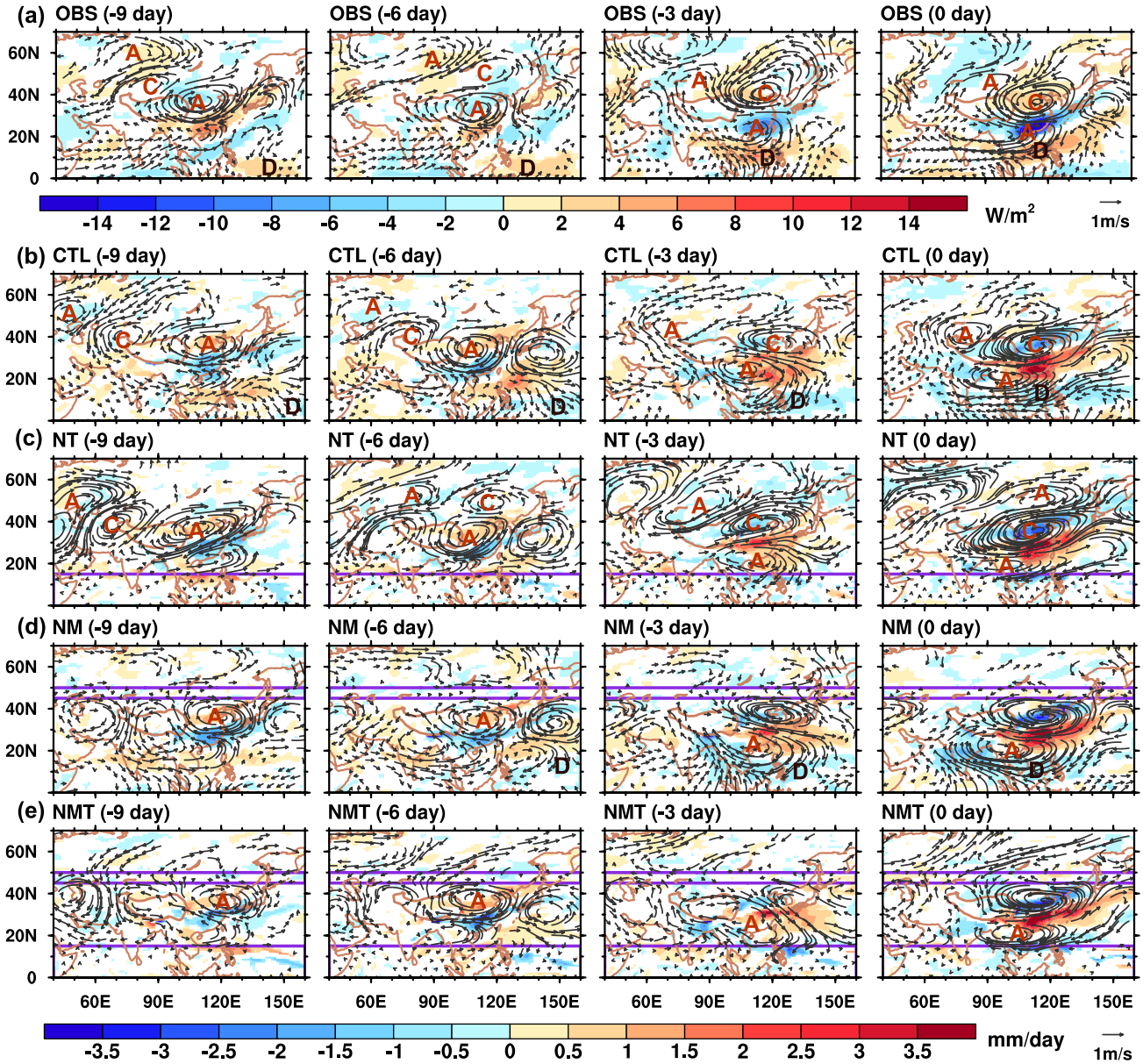

Figure 2. Origin and propagation of the first intraseasonal variability mode of East Asian summer precipitation. (a) Lagged regressions of intraseasonal outgoing longwave radiation (OLR) anomalies (shading; W m^{-2}) and 200 hPa wind anomalies (vector; m s^{-1}) against principal component1 for the summers of 1979–2005 in observations. Shading and vectors denote significant OLR anomalies and wind anomalies (either zonal or meridional wind) at the 95% confidence level. Thick orange contour indicates the elevation of 3,000 m. Letter A tracks the center of anomalous anticyclone; C, the cyclone; and D, the dry phase of intraseasonal oscillation. 8–40-day bandpass filter is performed before calculating the regressions. (b) Same as (a), except for control experiment (CTL); and shading denotes precipitation anomaly (mm day^{-1}). (c)–(e) Same as (b), except for the regressions onto the time series projected onto empirical orthogonal function1 of CTL in no tropical forcing (NT), no mid-to-high latitude forcing (NM), and no mid-to-high latitude and tropical forcings (NMT) runs. The solid purple lines indicate the nudging area.

3.2. Impacts of Mid-to-High Latitude and Tropical Forcings

In observations (Figure 2a), a preceding significant mid-to-high latitude wave train is observed from western Siberia, via Mongolia and Northeast Asia, toward Southeast China before the peak wet phase over Southeast China for the first ISV mode. In the tropics, however, a preceding westward propagation is observed. Significant preceding negative convection anomalies propagate from the western equatorial Pacific at day −9 to the South China Sea at day 0. At day 0, the enhanced precipitation from Southeast China to South Japan is related to this lower-tropospheric anticyclonic anomaly over the South China Sea and the upper-tropospheric anticyclone-induced upward motion.

Before the peak wet phase of second ISV mode over the lower reach of the Yangtze River and South Japan (Figure S3a in Supporting Information S1), a significant preceding mid-to-high latitude wave train from western Siberia, via southern Lake Baikal and Northeast Asia, toward Southeast China is also observed, along with the northwestward propagation of negative tropical convection anomaly from the western equatorial Pacific to Southeast China. These significant preceding mid-to-high latitude and tropical signals demonstrate the potential roles of external influence from mid-to-high latitude wave train and tropical ISO in these leading ISV modes of EASP, as observed previously (F. Liu et al., 2020b; Yang et al., 2010).

In CTL, significant preceding signals in the mid-to-high latitudes and the tropics are also simulated for the first (Figure 2b) and second (Figure S3b in Supporting Information S1) modes, consistent with observations (Figure 2a and Figure S3a in Supporting Information S1). However, the pathways are somehow different, with the preceding mid-to-high latitude wave trains from the Ural Mountain, via western Mongolia and Northeast Asia, toward South China for the first mode (Figure 2b), and from western Siberia, via Lake Baikal and Northeast Asia, toward East China for the second mode (Figure S3b in Supporting Information S1). The downstream response to the east of Japan is also stronger than that in the observation. The northwestward propagating tropical ISO's wet phase in front of dry phase is also stronger than that in the observation. Despite these model-observation differences, the CTL run of the CESM performs well in simulating the two leading ISV modes of EASP in terms of their spatial patterns, periods, and associated preceding signals in both mid-to-high latitudes and tropics. The actual phases of these leading modes cannot be simulated without performing hindcast experiments (Vitart et al., 2017).

In the NT run where the intraseasonal signals over the tropical band are suppressed, the first and second ISV modes are mainly related to the preceding mid-to-high latitude wave trains, and the northwestward propagation from the western equatorial Pacific to the South China Sea no longer occurs in the simulation (Figure 2c and Figure S3c in Supporting Information S1). On the other hand, in the NM run where the external forcing over the mid-to-high latitudes is prohibited, these two leading modes are related to the preceding northwestward propagation from the western equatorial Pacific to the South China Sea, while the signals in the mid-to-high latitudes are substantially weakened compared to those in CTL (Figure 2d and Figure S3d in Supporting Information S1). The preceding intraseasonal signals are feeble in both the tropics and the mid-to-high latitudes when the influences from both the tropical ISO and the mid-to-high latitude wave trains are suppressed in the NMT run (Figure 2e and Figure S3e in Supporting Information S1). The southward propagation is simulated over the monsoon band from 15° to 45°N for the two leading modes, suggesting upstream impacts on the EASP ISV. This simulated southward propagation may be due to the monsoon convection-circulation coupling and needs further investigation.

Compared to the CTL run, the variance for the first two leading ISV modes of EASP in the NT run is reduced (Figure 3), and the total ISV (8–40-day) reductions are 31% and 40% for these two modes, respectively (Table 1). Same reductions are also seen in the NM run, except that the variance for high-frequency (10–14-day) ISV of the second mode is enhanced compared to that in CTL. The total ISV variances are reduced by 24% and 15% accordingly. In the NMT run where both tropical and mid-to-high latitude forcings are removed, the EASP ISV is heavily suppressed for both leading modes, and the reduction reaches 53% for the first mode and 40% for the second mode. Similar results are obtained when considering the full intraseasonal band calculated by removing daily climatology and then performing 5-day running mean (Table S1 in Supporting Information S1).

Our simulation results quantify the contributions of external forcings from the mid-to-high latitude wave trains and the tropical ISO to EASP ISV. In the CESM, the tropical forcing contributes more (31%, 40% reductions for the first and second modes) than the mid-to-high latitude forcing (24%, 15%), and these external tropical and extratropical forcings together contribute to about half (53%, 40%) of the total variance. The remaining EASP ISV may come from local variability or upstream influences along the same latitude.

3.3. External Forcings Versus Local Variability

The leading ISV modes of EASP mainly represent the precipitation variability of regional pattern rather than the value at a localized grid (Figure 1). We then investigate how much the tropical and mid-to-high latitude forcings can affect the EASP ISV on different spatial scales. Let us first examine the change in ISV intensity on the local (grid) scale. In the CTL run, the centers of EASP ISV are located over coastal South China, eastern Tibetan Plateau, middle-to-lower reaches of the Yangtze River valley, North China, North Korea, and South Japan (Figure 4a). In the NMT run, the ISV intensity is significantly enhanced over eastern Tibetan Plateau, East China,

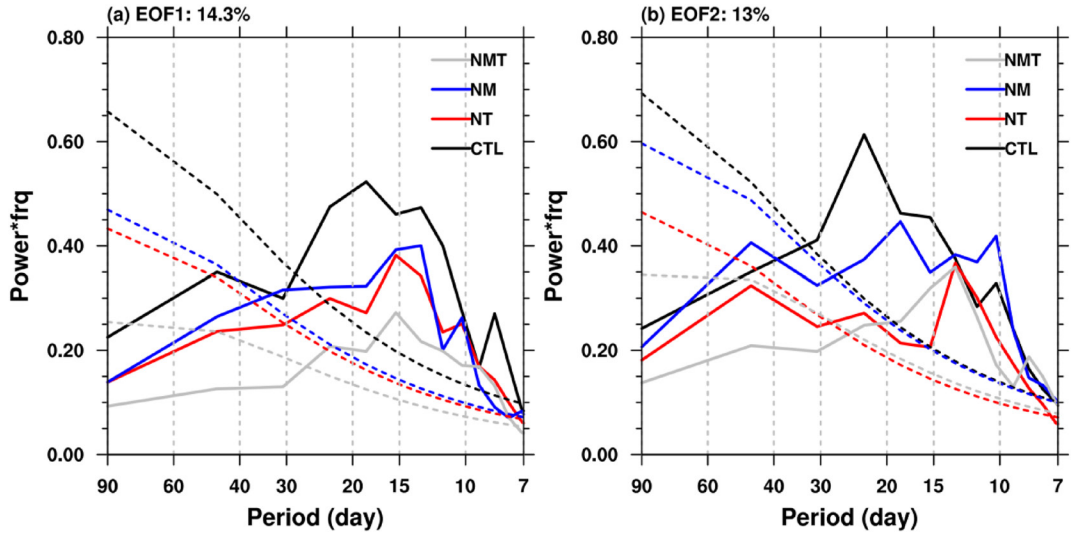

Figure 3. Mean power spectra of the (a) empirical orthogonal function EOF1 and (b) EOF2 modes of East Asian summer precipitation showing the power changes due to removing the midlatitude and tropical forcings. The spectra were obtained from the control experiment (CTL; black), no tropical forcing (NT; red), no mid-to-high latitude forcing (NM; blue), and no mid-to-high latitude and tropical forcings (NMT; gray) runs for the summers of 1979–2005. Dashed lines denote the corresponding 95% confidence level. The principal components (principal component [PC]1 and PC2) were used in CTL, while the projected time series onto the leading EOFs of CTL were used in NT, NM, and NMT runs.

eastern part of Northeast China, and North Japan (Figure 4b), meaning that the ISV intensity of precipitation on localized small scale is strengthened when both the tropical and mid-to-high latitude forcings are blocked, in contrast to the weakened dominant ISV modes (Figure 3). These enhanced ISV intensities are related to enhanced mean precipitation (Figure S2d in Supporting Information S1), demonstrating the mean-state control on the localized ISV intensity. The cause of increased seasonal-mean precipitation is unknown, which is beyond the scope of this work and should be analyzed by future investigations.

A spatial average with different smooth radii is used to derive the regionally averaged precipitation anomaly before calculating the ISV variance. When considering the regional scale with 400 km-radius smoothing (Figure 4c), the ISV intensity is weakened over most of East Asia except for South Korea and North Japan, which means that the ISV intensity of the regionally averaged precipitation is reduced when the tropical and mid-to-high latitude forcings are both obstructed. When focusing on the typical region located at the lower reach of the Yangtze River (118°E, 32°N), the changes in ISV intensity vary with spatial scale (Figure 4d): ISV intensity is enhanced by 38% on the scale less than 100 km radius, but weakened when the scale is larger than 250 km radius. The role of external tropical and mid-to-high latitude forcing prohibition in weakening the EASP ISV is increased when the target spatial scale increases.

The EASP ISV intensity increases on a local scale, while it decreases on a regional scale, meaning that the ISV phases are not correlated among individual grids of the monsoon region. The amplitude of ISV over each grid can be enhanced through local processes, while the possibility of all these grids exhibiting the same wet or dry phases is decreased when the large-scale external forcing is prohibited.

4. Concluding Remarks

In this work, we designed a set of sensitivity experiments with the CESM by using a grid nudging method to block the external forcings from the tropics and mid-to-high latitudes, allowing confirmation and quantification of the relative roles of tropical and mid-to-high latitude forcings in EASP ISV. The two leading ISV modes of EASP are related to a preceding mid-to-high latitude wave train and tropical northwestward propagating ISO from the western equatorial Pacific to the South China Sea (Figure 2). The CTL run can simulate these characteristics realistically although the simulated pathways of the mid-to-high latitude wave trains are a little different from the observations. When the tropical and mid-to-high latitude forcings are removed, these preceding signals

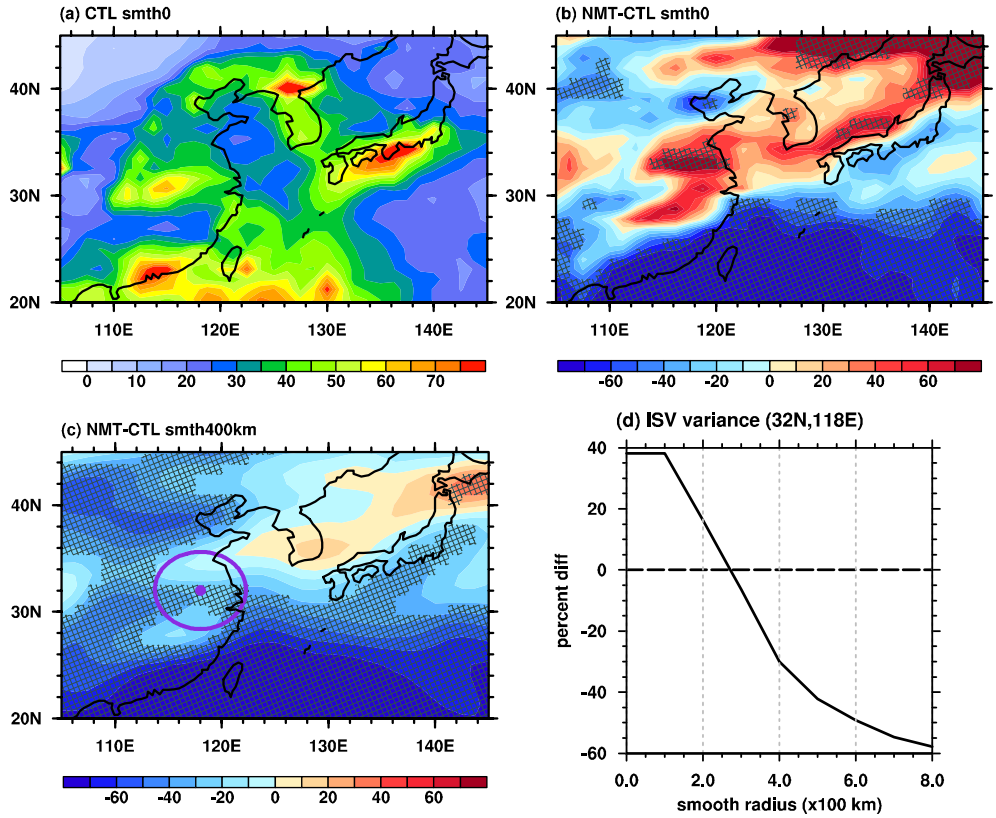

Figure 4. Change in East Asian summer precipitation intraseasonal variability on different spatial scales. (a) JJA intraseasonal precipitation variance ($mm^2\ day^{-2}$) in control experiment (CTL). (b) Difference of JJA intraseasonal precipitation variance (units in percentage change) between no mid-to-high latitude and tropical forcings (NMT) and CTL. Anomalies significant at the 95% confidence level are hatched. (c) Same as (b), except that a spatial smoothing with a radius of 400 km is performed for calculating intraseasonal precipitation anomaly over each grid. Purple circle encloses the area with a radius of 400 km used to calculate precipitation average for a selected grid (118°E, 32°N; purple dot). (d) Difference of JJA intraseasonal precipitation variance (units in percentage change) over the selected dot in c between NMT and CTL versus different radii used for spatial smoothing.

are substantially weakened, resulting in suppressed EASP ISV. The tropical forcing contributes more (31%, 40%) to the first two leading ISV modes of EASP than the mid-latitude forcing (24%, 15%). When both tropical and mid-to-high latitude forcings are blocked, these two leading modes are weakened by 53% and 40%, respectively. Our results suggest that improving tropical-extratropical interaction in an operation model is indispensable for better subseasonal prediction of EASP.

The enhanced local ISV intensity against the suppressed leading ISV modes challenges our current understanding of subseasonal prediction (Figure 4). Blocking external forcings from mid-to-high latitude wave train and tropical ISO only weakens the EASP ISV mainly on regional scale, rather than on a local (grid) scale. The results imply that we can only improve subseasonal prediction of regional mean precipitation based on the improved simulation of tropical ISO and midlatitude wave train, but not local precipitation.

The relative roles of tropical and mid-to-high latitude forcings in the EASP ISV obtained in this work can be model dependent to various degrees, which will be studied in the future. In this work, the external forcing from tropics and mid-to-high latitudes also includes the synoptic scale. Here, we only consider the linear process from the ISV itself; the nonlinear process from the synoptic forcing should be studied by nudging 8-day lowpass-filtered field in the future.

Data Availability Statement

The APHRO_MA_025deg_V1003R1 data were available from https://iridl.ldeo.columbia.edu/SOURCES/.RIHN/.aphrodite/.V1003R1/.APHRO_MA_025deg/. Daily OLR data were downloaded from https://psl.noaa.gov/data/gridded/data.olrcdr.interp.html. Daily ERA-Interim reanalysis data were retrieved from https://apps.ecmwf.int/datasets/data/interim-full-daily/levtype=pl/.

Acknowledgments
This work was jointly funded by the Guangdong Major Project of Basic and Applied Basic Research (Grant 2020B0301030004), the National Natural Science Foundation of China (No. 42088101), the Natural Science Foundation of China (Grant 41975107, 42175061), and the Guangdong Province Key Laboratory for Climate Change and Natural Disaster Studies (Grant 2020B1212060025). Bin Wang. acknowledges the support from the National Science Foundation (Award number 2025057).

References

Blackmon, M., Lee, Y. H., Wallace, J., & Hsu, H. H. (1984). Time variation of 500 mb height fluctuations with long, intermediate and short timescales as deduced from lag-correlation statistics. *Journal of the Atmospheric Sciences*, *41*(6), 981–991. https://doi.org/10.1175/1520-0469(1984)041<0981:tvomhf>2.0.co;2

Cao, X., Ren, X., & Yang, X. (2012). The quasi-biweekly oscillation characteristics of persistent severe rain and its general circulation anomaly over southeast China from May to August. *Acta Meteorologica Sinica*, *70*(4), 766–778. https://doi.org/10.11676/qxxb2012.062

Chen, L. X., Zhu, C. W., Wang, W., & Zhang, P. Q. (2001). Analysis of the characteristics of 30–60 day low-frequency oscillation over Asia during 1998 SCSMEX. *Advances in Atmospheric Sciences*, *18*(4), 623–638. https://doi.org/10.1007/s00376-001-0050-0

Dee, D. P., Uppala, S. M., Simmons, A. J., Berrisford, P., Poli, P., Kobayashi, S., et al. (2011). The ERA-interim reanalysis: Configuration and performance of the data assimilation system. *Quarterly Journal of the Royal Meteorological Society*, *137*(656), 553–597. https://doi.org/10.1002/qj.828

DeMott, C., Klingaman, N., & Woolnough, S. (2015). Atmosphere-ocean coupled processes in the Madden-Julian oscillation. *Reviews of Geophysics*, *53*(4), 1099–1154. https://doi.org/10.1002/2014RG000478

Ding, Y., Liu, Y., & Hu, Z. Z. (2021). The record-breaking meiyu in 2020 and associated atmospheric circulation and tropical SST anomalies. *Advances in Atmospheric Sciences*, *38*, 1980–1993. https://doi.org/10.1007/s00376-021-0361-2

Gao, M., Yang, J., Wang, B., Zhou, S., Gong, D., & Kim, S. J. (2018). How are heat waves over Yangtze River valley associated with atmospheric quasi-biweekly oscillation? *Climate Dynamics*, *51*(11–12), 4421–4437. https://doi.org/10.1007/s00382-017-3526-z

Gates, W. (1992). AMIP: The Atmospheric Model Intercomparison project. *Bulletin of the American Meteorological Society*, *73*(12), 1962–1970. https://doi.org/10.1175/1520-0477(1992)073<1962:atamip>2.0.co;2

Gilman, D., Fuglister, F., & Jr, M. (1963). On the power spectrum of "red noise". *Journal of the Atmospheric Sciences*, *20*(2), 182–184. https://doi.org/10.1175/1520-0469(1963)020<0182:otpson>2.0.co;2

Huang, F., Huang, S. N., & Zhang, X. (2008). Study on the climatological intraseasonal oscillation of Chinese rainfall (in Chinese). *Periodical of Ocean University of China*, *38*(2), 173–177. https://doi.org/10.1007/s11442-008-0201-7

Hurrell, J. W., Hack, J., Shea, D., Caron, J., & Rosinski, J. (2008). A new sea surface temperature and sea ice boundary dataset for the Community Atmosphere Model. *Journal of Climate*, *21*(19), 5145–5153. https://doi.org/10.1175/2008JCLI2292.1

Hurrell, J. W., Holland, M., Gent, P., Ghan, S., Kay, J., Kushner, P., et al. (2013). The community Earth system model: A framework for collaborative research. *Bulletin of the American Meteorological Society*, *94*(9), 1339–1360. https://doi.org/10.1175/BAMS-D-12-00121.1

Jia, X., & Yang, S. (2013). Impact of the quasi-biweekly oscillation over the western North Pacific on East Asian subtropical monsoon during early summer. *Journal of Geophysical Research: Atmospheres*, *118*(10), 4421–4434. https://doi.org/10.1002/jgrd.50422

Jia, X., Yang, S., Li, X., Liu, Y., Wang, H., Liu, X., & Weaver, S. (2013). Prediction of global patterns of dominant quasi-biweekly oscillation by the NCEP Climate Forecast System version 2. *Climate Dynamics*, *41*(5–6), 1635–1650. https://doi.org/10.1007/s00382-013-1877-7

Kikuchi, K., & Wang, B. (2009). Global perspective of the quasi-biweekly oscillation. *Journal of Climate*, *22*(6), 1340–1359. https://doi.org/10.1175/2008JCLI2368.1

Lee, J.-Y., Wang, B., Wheeler, M. C., Fu, X., Waliser, D. E., & Kang, I.-S. (2013). Real-time multivariate indices for the boreal summer intraseasonal oscillation over the Asian summer monsoon region. *Climate Dynamics*, *40*(1–2), 493–509. https://doi.org/10.1007/s00382-012-1544-4

Liang, P., & Ding, Y. (2012). Climatologic characteristics of the intraseasonal oscillation of East Asian meiyu (in Chinese). *Acta Meteorologica Sinica*, *70*(3), 418–435.

Liu, B., Yan, Y., Zhu, C. W., Ma, S., & Li, J. (2020). Record-breaking meiyu rainfall around Yangtze River in 2020 regulated by the subseasonal phase transition of North Atlantic oscillation. *Geophysical Research Letters*, *47*(22), e2020GL090342. https://doi.org/10.1029/2020GL090342

Liu, F., Ouyang, Y., Wang, B., Yang, J., Ling, J., & Hsu, P. C. (2020). Seasonal evolution of the intraseasonal variability of China summer precipitation. *Climate Dynamics*, *54*(11), 4641–4655. https://doi.org/10.1007/s00382-020-05251-0

Liu, F., & Wang, B. (2013). Mechanisms of global teleconnections associated with the Asian summer monsoon: An intermediate model analysis. *Journal of Climate*, *26*(5), 1791–1806. https://doi.org/10.1175/jcli-d-12-00243.1

Livezey, R. E., & Chen, W. Y. (1983). Statistical field significance and its determination by Monte Carlo techniques. *Monthly Weather Review*, *111*(1), 46–59. https://doi.org/10.1175/1520-0493(1983)111<0046:sfsaid>2.0.co;2

Lorenz, D., & Hartmann, D. (2001). Eddy–zonal flow feedback in the Southern Hemisphere. *Journal of the Atmospheric Sciences*, *58*(21), 3312–3327. https://doi.org/10.1175/1520-0469(2001)058<3312:ezffit>2.0.co;2

Madden, R. A., & Julian, P. R. (1971). Detection of a 40–50 day oscillation in the zonal wind in the tropical Pacific. *Journal of the Atmospheric Sciences*, *28*(5), 702–708. https://doi.org/10.1175/1520-0469(1971)028<0702:doadoi>2.0.co;2

Mao, J., & Chan, J. C. L. (2005). Intraseasonal variability of the South China Sea summer monsoon. *Journal of Climate*, *18*(13), 2388–2402. https://doi.org/10.1175/JCLI3395.1

Mao, J., & Wu, G. (2006). Intraseasonal variations of the Yangtze rainfall and its related atmospheric circulation features during the 1991 summer. *Climate Dynamics*, *27*(7), 815–830. https://doi.org/10.1007/s00382-006-0164-2

Meehl, G. A., Richter, J. H., Teng, H., Capotondi, A., Cobb, K., Doblas-Reyes, F., et al. (2021). Initialized Earth System prediction from subseasonal to decadal timescales. *Nature Reviews Earth & Environment*, *2*(5), 340–357. https://doi.org/10.1038/s43017-021-00155-x

North, G., Bell, T., Cahalan, R., & Moeng, F. (1982). Sampling errors in the estimation of empirical orthogonal functions. *Monthly Weather Review*, *110*(7), 699–706. https://doi.org/10.1175/1520-0493(1982)110<0699:SEITEO>2.0.CO;2

Qi, X., Yang, J., Gao, M., Yang, H., & Liu, H. (2019). Roles of the tropical/extratropical intraseasonal oscillations on generating the heat wave over Yangtze River valley: A numerical study. *Journal of Geophysical Research: Atmospheres*, *124*(6), 3110–3123. https://doi.org/10.1029/2018JD029868

Ren, P., Ren, H., Fu, J. X., Wu, J., & Du, L. (2018). Impact of boreal summer intraseasonal oscillation on rainfall extremes in southeastern China and its predictability in CFSv2. *Journal of Geophysical Research: Atmospheres*, *123*(9), 4423–4442. https://doi.org/10.1029/2017JD028043

Ren, Q., Jiang, X., Zhang, Y., Li, Z., & Yang, S. (2021). Effects of suppressed transient eddies by the Tibetan Plateau on the East Asian summer monsoon. *Journal of Climate*, *34*(21), 8481–8501. https://doi.org/10.1175/JCLI-D-20-0646.1

Simmons, A., Wallace, J., & Branstator, G. (1983). Barotropic wave propagation and instability, and atmospheric teleconnection patterns. *Journal of the Atmospheric Sciences*, *40*(6), 1363–1392. https://doi.org/10.1175/1520-0469(1983)040<1363:bwpaia>2.0.co;2

Vitart, F., Ardilouze, C., Bonet, A., Brookshaw, A., Chen, M., Codorean, C., et al. (2017). The Subseasonal to Seasonal (S2S) prediction project database. *Bulletin of the American Meteorological Society*, *98*(1), 163–173. https://doi.org/10.1175/bams-d-16-0017.1

Wang, B., Huang, F., Wu, Z., Yang, J., Fu, X., & Kikuchi, K. (2009). Multi-scale climate variability of the south China sea monsoon: A review. *Dynamics of Atmospheres and Oceans*, *47*(1–3), 15–37. https://doi.org/10.1016/j.dynatmoce.2008.09.004

Wang, M., Wang, J., Duan, A., Liu, Y., & Zhou, S. (2018). Coupling of the quasi-biweekly oscillation of the Tibetan Plateau summer monsoon with the Arctic oscillation. *Geophysical Research Letters*, *45*(15), 7756–7764. https://doi.org/10.1029/2018GL077136

Wei, L., Fang, J., & Yang, X. (2017). Low-frequency oscillation characteristics of 12–30 d persistent heavy rainfall over South China (in Chinese). *Acta Meteorologica Sinica*, *75*(1), 80–97. https://doi.org/10.11676/qxxb2017.008

Wheeler, M. C., & Hendon, H. H. (2004). An all-season real-time multivariate MJO index : Development of an index for monitoring and prediction. *Monthly Weather Review*, *132*(8), 1917–1932. https://doi.org/10.1175/1520-0493(2004)132<1917:aarmmi>2.0.co;2

Yang, J., Bao, Q., Wang, B., He, H., Gao, M., & Gong, D. (2017). Characterizing two types of transient intraseasonal oscillations in the eastern Tibetan Plateau summer rainfall. *Climate Dynamics*, *48*(5), 1749–1768. https://doi.org/10.1007/s00382-016-3170-z

Yang, J., Wang, B., Bao, Q., & Bao, Q. (2010). Biweekly and 21–30-Day variations of the subtropical summer monsoon rainfall over the lower reach of the Yangtze River Basin. *Journal of Climate*, *23*(5), 1146–1159. https://doi.org/10.1175/2009jcli3005.1

Yatagai, A., Kamiguchi, K., Arakawa, O., Hamada, A., Yasutomi, N., & Kitoh, A. (2012). APHRODITE: Constructing a long-term daily gridded precipitation dataset for Asia based on a dense network of rain gauges. *Bulletin of the American Meteorological Society*, *93*(9), 1401–1415. https://doi.org/10.1175/BAMS-D-11-00122.1

Zangvil, A. (1977). On the presentation and interpretation of spectra of large-scale disturbances. *Monthly Weather Review*, *105*(11), 1469–1472. https://doi.org/10.1175/1520-0493(1977)105<1469:OTPAIO>2.0.CO;2

Zhang, Y., Yang, X.-Q., Nie, Y., & Chen, G. (2012). Annular Mode-like variation in a multilayer quasigeostrophic model. *Journal of the Atmospheric Sciences*, *69*, 2940–2958. https://doi.org/10.1175/JAS-D-11-0214.1